JGR Space Physics

RESEARCH ARTICLE
10.1029/2025JA034462

Key Points:

- A 3D Model of O^{7+} soft X-ray emission in Saturn's equatorial magnetosheath is developed
- Intensity of emission is dictated primarily by neutral density profile
- Integration times show imaging of soft X-ray emission region as a point source is likely to be viable

Correspondence to:

L. C. Ray,
licia.ray@lancaster.ac.uk

Citation:

Rogan, P. C., Ray, L. C., Naylor, D., Dunn, W. R., Jia, X., Smith, H. T., & Sulaiman, A. (2026). Soft X-ray emission from Saturn's magnetosheath part I: 3D modeling from MHD data. *Journal of Geophysical Research: Space Physics*, *131*, e2025JA034462. https://doi.org/10.1029/2025JA034462

Received 17 JUL 2025
Accepted 27 APR 2026

Author Contributions:

Conceptualization: P. C. Rogan, L. C. Ray, W. R. Dunn
Data curation: P. C. Rogan, X. Jia, H. T. Smith, A. Sulaiman
Formal analysis: P. C. Rogan, L. C. Ray, D. Naylor, W. R. Dunn, H. T. Smith, A. Sulaiman
Investigation: P. C. Rogan, L. C. Ray
Methodology: P. C. Rogan, L. C. Ray, D. Naylor, H. T. Smith
Project administration: L. C. Ray
Resources: L. C. Ray, X. Jia
Software: P. C. Rogan
Supervision: L. C. Ray
Validation: P. C. Rogan, D. Naylor
Writing – original draft: P. C. Rogan
Writing – review & editing: P. C. Rogan, L. C. Ray, D. Naylor, W. R. Dunn, X. Jia, H. T. Smith, A. Sulaiman

Soft X-Ray Emission From Saturn's Magnetosheath Part I: 3D Modeling From MHD Data

P. C. Rogan[1,2], L. C. Ray[1], D. Naylor[1], W. R. Dunn[3], X. Jia[4], H. T. Smith[5], and A. Sulaiman[6]

[1]Department of Physics, Space and Planetary Physics Group, Lancaster University, Lancaster, UK, [2]Now at Institute for Geophysics and Meteorology, University of Cologne, Cologne, Germany, [3]Department of Physics & Astronomy, University College London, London, UK, [4]Department of Climate and Space Sciences and Engineering, University of Michigan, Ann Arbor, MI, USA, [5]Johns Hopkins University Applied Physics Laboratory, Space Physics Group, Space Exploration Sector, Laurel, MD, USA, [6]School of Physics and Astronomy, Minnesota Institute for Astrophysics, University of Minnesota, Minneapolis, MN, USA

Abstract Saturn's magnetosheath hosts a mixed population of water-group neutrals and solar wind plasma. We present a 3-D model of soft X-ray emission by ion-neutral charge exchange in the near-equatorial magnetosheath. The model employs MHD simulation data of plasma properties at Saturn, Enceladus-genic neutral populations extrapolated from existing physical chemistry models, and circumscribes the magnetosheath region using existing magnetopause and bow shock models. Emission is concentrated in the equatorial plane and toward the magnetosheath nose, with volumetric emission rates of 10^{-10}–10^{-11} photons $\mathrm{cm}^{-3}\ \mathrm{s}^{-1}$. We explore viable imaging distances for a SMILE-like instrument. We conclude that imaging of Saturn's magnetopause is viable within 40 R_S, with integration times on the order of ∼1 min. However, the SMILE SXI field of view would only image 0.5% of the emission region at this distance. Enhancements in effective area comparable to MIXS on BepiColombo or closer viewing with a wider field of view would enable the whole magnetosheath to be imaged on few-minute timescales. Soft X-ray emission observations can be used to study the location, structure, and global dynamics of the magnetosheath region, and to inform neutral density models, especially of the outer system. Finally, far viewing of the emission region as a point source may be sufficient to capture variability in emission rate driven both by Saturn's internal plasma environment and varying solar wind conditions.

Plain Language Summary Water plumes at the south pole of Enceladus supply the space around Saturn with a mix of neutral particles, including H_2O, OH, oxygen, and hydrogen. These disperse out to the magnetosheath, a region of space where the solar wind meets Saturn's magnetic field. Here, these neutrals collide with highly ionized oxygen in the solar wind to emit X-rays via a process known as charge exchange. We employ an MHD (magnetohydrodynamic) model, which simulates the flow of the solar wind like a fluid around Saturn's magnetic field, and produce a 3D map of the X-ray emission generated. We explore whether this emission is bright enough to be captured by a probe equipped with a soft X-ray imager (SXI), sensitive to the X-rays we expect, and find that while the X-ray emission is bright enough to be visible, integration times are too long to easily generate an "instantaneous" map of the system.

1. Introduction

Detailed characterization of the space environment around Saturn by Cassini revealed a magnetosphere rich in both neutrals and plasma, with clouds and structures stretching far into the outer Kronian system (Smith et al., 2010; Thomsen et al., 2010). The cryovolcanic plumes of Enceladus are the primary internal mass source for neutrals (Smith & Richardson, 2021), while plasma is supplied both by the solar wind and by the ionisation of neutrals in the system (Allen et al., 2018). Saturn and its rings are also considerable neutral sources in the inner system (Shemansky et al., 2009), while other satellites like Titan provide marginal local contributions further out (Tseng et al., 2013). However, while these populations and their impacts are very well characterized in the inner system, dynamic behavior in the outer system makes neutral densities near the magnetosheath more variable (Smith & Richardson, 2021). As a result, better characterization of the outer system neutrals is a current research goal.

The location of the magnetopause is determined by the balance between internal pressure, from Saturn's magnetic field and magnetospheric plasma, and external pressure, supplied by the incident solar wind (e.g., Arridge et al., 2006). The magnetospheric plasma population strongly influences the dynamics of the system and the location of the magnetospheric boundary (Pilkington et al., 2015b). Rather than having a steady contribution, high and low pressure plasma structures appear to move periodically outward to the boundary region (Kivelson & Jia, 2014). This variation, together with changes in the incident solar wind pressure, leads to a boundary region whose location shifts considerably in time (Achilleos et al., 2008). Tracking the boundary region's movement provides useful data on the processes that drive system behavior, many of which occur on timescales on the order of Saturn's rotation period ($T_S = 10.7$ hr, Clarke et al., 2010). The movement of the magnetopause boundary, and the magnetosheath region with it, can be used to study the varying influence of internal and external pressure sources.

Tracking the location of the magnetopause and bow shock boundaries has historically required in situ measurement, as was performed by Cassini (e.g., Jackman et al., 2019; Kanani et al., 2010; Pilkington et al., 2015a). However, such methods are necessarily limited in spatial coverage. Soft X-ray imaging is an emerging tool for locating and characterizing regions of mixed neutral and charged populations (e.g., Bodewits, et al., 2007; Whittaker et al., 2016, etc.), with the potential to become a powerful global imaging tool. As the magnetosheath of Saturn is rich in both neutrals from internal sources and energetic charged particles supplied by the solar wind, it is likely to be a strong local source of soft X-rays (SX) generated via charge exchange (Whittaker et al., 2016), with "soft" denoting X-rays in the energy range of $0.2-1.1$ keV (Sembay et al., 2024; Yoshino et al., 2009).

These methods have already been deployed with XMM Newton to study Earth's magnetosphere (Carter & Sembay, 2008; Carter et al., 2011), and future deployments on missions like SMILE will track variations in Earth's magnetospheric regions in more detail (Raab et al., 2016). Beyond Earth, outer planetary systems where rich moon-derived neutral populations exist are candidates for similar analysis. Previous studies have shown that Jupiter is unlikely to possess significant emission structures due to the sheer scale of its magnetosphere, which places its magnetosheath far outside the regions of substantial neutral density (Leppard et al., 2025). However, Uranus is a promising candidate for further soft X-ray investigations, depending on the density of neutrals present within the system (Naylor et al., 2025). Thus, soft X-ray imaging can be combined with accurate solar wind data and propagation models to provide an improved global picture of neutral densities within a planetary magnetosheath. Soft X-ray imaging also can be used to characterize the periodic pressure sources that drive magnetopause dynamics. These objectives create a strong motivation to search for a candidate emission region at Saturn to constrain neutral density structures and inform periodic system behavior.

In this study we construct a 3D model of soft X-ray emission in Saturn's magnetosheath, in particular the near-equatorial region where neutral densities are better characterized. The focus of the study is charge exchange between water group neutrals (H, O, OH) originating from Enceladus and highly stripped O^{7+} oxygen ions, whose interactions lead to soft X-ray emission. Section 2 details the model used, whereby a previously-developed global MHD model of the incident solar wind flow around Saturn and a model of the diffusion of water group neutrals to the outer system are used to establish neutral and charge densities and relative interaction velocities in the magnetosheath. Section 3 describes the calculation of the volumetric emission rate and the results. Section 4 discusses the potential to image the emission region with current technology. Section 5 presents a discussion of these results and avenues for future work before concluding in Section 6.

2. Magnetosheath Model

2.1. MHD Simulation

The model uses 3D magneto-hydrodynamic (MHD) simulation data of the incident solar wind flow at Saturn, which encounters, is compressed by, and flows around Saturn's magnetic field. The magnetopause marks the boundary between the magnetosphere, where Saturn's magnetic field dominates, and interplanetary space, where the solar wind is dominant. The bow shock sits several R_S (1 Saturn radius (R_S) $= 60,268$ km) upstream of the magnetopause, where the incident supersonic solar wind plasma is shocked as it approaches the upstream obstacle of the magnetosphere and begins to pile up and slow down. The magnetosheath lies between these two boundary surfaces and is the region where significant soft X-ray emission is most likely to occur. Each point in the MHD data set is described in KSM (Kronocentric Solar Magnetospheric) coordinates, where the positive X_{KSM} axis points sunward, the X_{KSM}-Z_{KSM} plane contains the Kronian magnetic dipole axis, and the positive Y_{KSM} axis completes a right-handed set.

Table 1
Values of Dimensionless Parameters in Magnetopause Empirical Models

Parameter	Value
a_1	10.3
a_2	0.2
a_3	0.73
a_4	0.4
a_5	0.024

The MHD simulation data was obtained from Sulaiman et al. (2017) based on work originally by Jia et al. (2012). This simulation uses the global 3D MHD model BATS-R-US (Gombosi, Tamas I. et al., 2021), solving the MHD equations on a non-uniform spherical mesh. Saturn lies in the ecliptic plane, such that the incident solar wind flow is normal to the Kronian magnetic dipole axis, and in the negative X_{KSM} direction. The MHD model outputs the mass density, flow velocity, magnetic field strength, and plasma pressure at every point in the system. The simulation considers a steady incident solar wind, with bulk flow velocity $v_{SW} = 490\ \text{km s}^{-1}$ and number density $n_{SW} = 0.09\ \text{cm}^{-3}$. Assuming the solar wind is composed almost entirely of protons and electrons, the mass density in amu cm^{-3} is approximately equal to the number density of protons in cm^{-3}.

The dynamic pressure D_P of the incident solar wind is calculated by

$$D_P = n_{SW} m_P v_{SW}^2 \tag{1}$$

where m_p is the mass of a proton. This dynamic solar wind pressure then defines the magnetopause standoff distance, and in turn the magnetopause surface, via an empirical model developed by Kanani et al. (2010) with modifications from Pilkington et al. (2014, 2015a). The magnetopause standoff distance at the nose $(Y_{KSM}, Z_{KSM} = 0)$ r_0, and the pressure-dependent flaring parameter, K are defined as

$$r_0 = a_1 D_P^{-a_2} \tag{2}$$

$$K = a_3 + a_4 D_P + a_5 \cos\phi \tag{3}$$

Pilkington et al. (2015a) introduces the extra $a_5 \cos\phi$ term to create a dawn-dusk asymmetry, where ϕ is the angle between the Y_{KSM} axis and the radial projection of the position vector onto the YZ_{KSM} plane. This angular dependence gives $\cos\phi$ values of 1 at dawn, -1 at dusk, and 0 at the poles, such that the flaring parameter K at dawn and dusk differ by a factor of $2a_5$, while K in the Z_{KSM} direction is unaffected. The final empirical magnetopause equation has the form

$$r_{MP} = r_0 \left(\frac{2}{1 + \cos\theta}\right)^{a_3 + a_4 D_P + a_5 \cos\phi} \tag{4}$$

where r_{MP} is the distance from planet to a point on magnetopause, and θ is the angle between the point's position vector and the x axis. Values for the model parameters used in Equations 2–4 are given in Table 1.

Due to the effect of Saturn's magnetodisc, the magnetopause is confined along the poles by 19% compared to at the equator (Pilkington et al., 2014). This effect is parametrized by a polar confinement factor $\varepsilon = 0.81$, such that the magnetopause z coordinate is calculated as

$$z_{MP} = \varepsilon y_{MP} \tag{5}$$

The outer bow shock boundary is imposed by discontinuities in the magnetic field strength and number density, which drop considerably at the bow shock boundary (Sulaiman et al., 2017; Went et al., 2011). Since the number density declines on both sides of the bow shock, the additional magnetic field condition prevents loss of data points inside the magnetosheath. All outer points with field strength below observed cut-offs of 1.08 nT and number density below $0.26\ \text{cm}^{-3}$, and all points lying inside the empirical magnetopause boundary, are removed from the original 3D MHD data cube. The modeling domain is restricted to $\pm 10\ R_S$ above and below the equator, where neutral density is well-constrained. The final product is a 3D map of the near-equatorial magnetosheath region, with values for plasma number density, flow velocity, magnetic field, and plasma pressure.

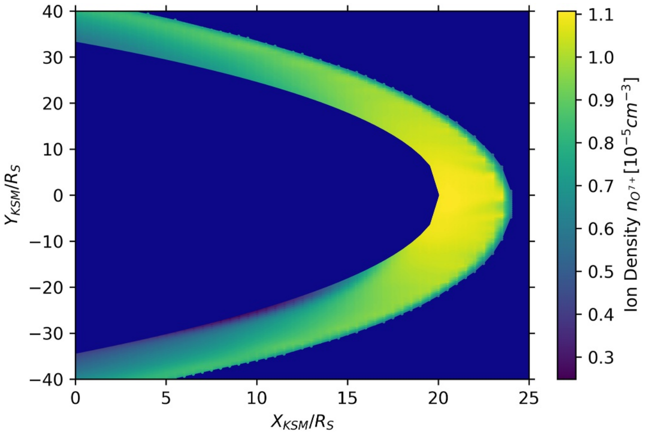

Figure 1. Incident solar wind O^{7+} ion density in Saturn's magnetosheath, determined by scaling MHD proton densities. Saturn lies at (0, 0), and the positive X direction is sunward.

Soft X-rays are produced by charge exchange between highly stripped ions and neutrals. MHD simulation data provides the mass density of ions in the magnetosheath in amu cm^{-3}. Assuming the solar wind is composed almost entirely of protons and electrons, this mass density approximately equals the number density of protons in the magnetosheath region. Composition and ionisation data for the solar wind from ACE (Advanced Composition Explorer) is then used to convert proton density into the equivalent density of O^{7+}, with the full set of assumptions described in Section 3. Figure 1 shows the shape of the simulated region in the equatorial plane, constrained by the inner boundary of the magnetopause and the outer boundary of the bow shock, as well as the spatial profile of O^{7+}.

2.2. Neutral Density

Enceladus-genic neutral densities in the magnetosheath are determined by the model of Smith and Richardson (2021). The neutral densities reflect an effectively constant mass ejection rate, as temporal variations occur on much shorter timescales than Enceladus's orbital period. Additionally, the OH, O, and H densities in the outer system imposed are approximately symmetric in the equatorial plane, as water-group neutrals spread outward. We consider Saturn at equinox, such that in the KSM coordinate system the equatorial plane and neutral population intersect at the nose of the magnetosheath that is, $Y_{KSM} = 0, Z_{KSM} = 0$.

The density of all water group neutral species peaks at a distance of ~4 R_S from Saturn, the orbital radius of Enceladus, then declines moving outward. Exponential fits are applied to the modeled neutral densities outside 10 R_S, with radial density profiles of H, O, OH, and H_2O extrapolated to distances of 50 R_S. H_2O density declines quickly with radial distance and is negligible at typical magnetosheath distances; it is thus not expected to contribute significantly to X-ray emission rates and neglected moving forward. The neutral scale height, as a function of radius, is informed by a fit to the vertical distribution of each neutral species (Smith & Richardson, 2021). The resulting function is

$$n_X = a_X e^{-b_X r} e^{-z/z_{0,X}(r)} \tag{6}$$

where n_X is the neutral density of species X, r is the equatorial distance, z is the height above the equatorial plane, $z_{0,X}(r)$ is the scale height of species X at r, and a_X, b_X are fitting parameters. The full parameters for equation 2.2 and functions for $z_{0,X}(r)$ are provided in Table 2.

Figure 2 shows neutral density and scale height as a function of equatorial radius. The density of each relevant species can then be determined for every point in the magnetosheath, and summed to give the total neutral density at each point.

3. Volumetric Emission Rates

The calculation of soft X-ray emissivity in the magnetosheath follows the methodology set out in Whittaker et al. (2016), with some minor modifications. The volumetric emission rate of photons, P, measured in cm^{-3} s^{-1} is

$$P = n_n n_{H+} \beta v_{rel} \tag{7}$$

where n_n is the neutral density, n_{H+} is the proton density, v_{rel} is the relative velocity of the collision, and the parameter β is defined as

$$\beta = \sigma \left[\frac{\mathrm{O}}{\mathrm{H}}\right] \left[\frac{X^{q+}}{\mathrm{O}}\right] \tag{8}$$

encapsulating the cross-section σ of the interaction, the oxygen abundance $\left[\frac{\mathrm{O}}{\mathrm{H}}\right]$ in the solar wind, and the particular abundance $\left[\frac{X^{q+}}{\mathrm{O}}\right]$ of the O[Q+] ion in

Table 2
Values of Neutral Density Function Parameters

Species	a_X	b_X	$z_{0,X}(r)$	$a_{X,z}$	$b_{X,z}$	$c_{X,z}$
O	280	0.198	1	–	–	–
H	546	0.166	$a_{X,z} \log(z b_{X,z}) + c_{X,z}$	5.55	0.546	−6.02
OH	957	0.169	$a_{X,z} r^2 + b_{X,z} r + c_{X,z}$	0.0016	0.071	1.07

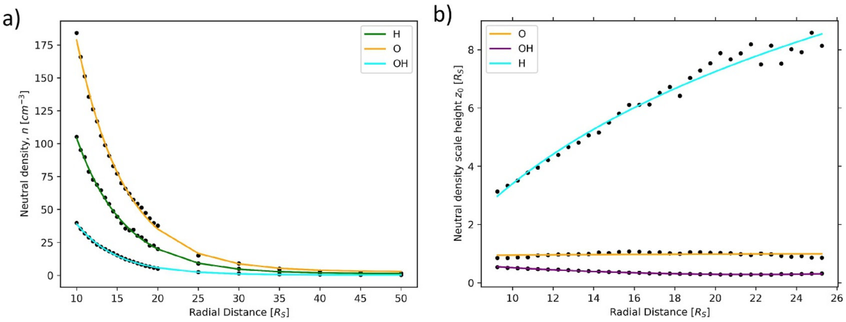

Figure 2. Magnetospheric (a) neutral density and (b) scale height data with fitted curves.

the oxygen population. For slow solar wind as is used in the MHD simulation, and therefore also in the magnetosheath, the abundance of oxygen is $\frac{O}{H} = 1.1 \times 10^{-3}$ and the ionisation fraction of O^{7+} is $\frac{X^{q+}}{O} = 0.28$ (Whittaker et al., 2016).

The relative collision velocity of the interaction includes contributions from both the bulk flow and thermal velocity. The combined average velocity (Whittaker et al., 2016) is

$$v_{tot} = \sqrt{v_{SH}^2 + \frac{3k_B T}{m_p}} \tag{9}$$

where v_{SH} is the bulk magnetosheath velocity, T is the temperature, m_p is the proton mass, and k_B is the Boltzmann constant. The average mass of magnetosheath plasma is assumed to be the proton mass, as the vast majority of solar wind ions are hydrogen. Using the plasma pressure, p, and density, ρ, (MHD model outputs) the plasma temperature T is:

$$T = \frac{p}{\rho}\frac{m_p}{k_B} \tag{10}$$

The plasma thermal velocity ranges from 380 km s^{-1} at the nose to 230 km s^{-1} at the flank, where the plasma is less compressed. This profile provides a significant contribution to the velocity in regions with slower bulk flow and a reduced effect in higher-velocity regions. The Keplerian orbital velocities of the neutral populations were found to have a negligible contribution to the relative collision velocity and neglected.

We focus on three charge exchange interactions: the z, xy, and w transitions of OVIII to OVII. Cross sections, σ, for interactions of highly stripped oxygen ions with hydrogen at relative collision velocities from 200 to 1,000 km s^{-1} range from $37 - 31 \times 10^{-16}$, $10 - 9.7 \times 10^{-16}$, and $9.9 - 11 \times 10^{-16}$ cm^{-2} for the z, xy, and w transitions respectively (Bodewits et al., 2007). We linearly interpolate between these values to calculate β throughout the magnetosheath for each transition, and sum to find a total β. The volumetric photon emission rate is then calculated at each location for each neutral species using Equation 7 and summed to give a total emission rate. For O and OH interactions with O^{7+}, we use the constant cross-section $\sigma = 120 \times 10^{-16}$ cm^{-2}, the total of all transitions (Schwadron & Cravens, 2000).

The emission region, shown in Figure 3, is a quasi-2D structure. The strongest emission is concentrated in the equatorial plane at the nose, decreasing with distance along the flanks and away from the equatorial plane. The peak emission rate is $P = 2.34 \times 10^{-9}$ cm^{-3} s^{-1} with a minimum of $P = 2.11 \times 10^{-11}$ cm^{-3} s^{-1} at the flank terminator $(X_{KSM} = 0)$, which is the edge of our modeling domain.

The spatial distribution of emission mirrors that of the neutral density, which varies by two orders of magnitude between the lowest emissivity region at the flank and the highest at the nose. In comparison the other factors contributing to emission are relatively uniform. The collision velocity is reduced by 20% at the nose relative to the flank, while the magnetosheath ion density is largely uniform, except for a slight enhancement at the nose and small decrease at the flank boundary (see Figure 1).

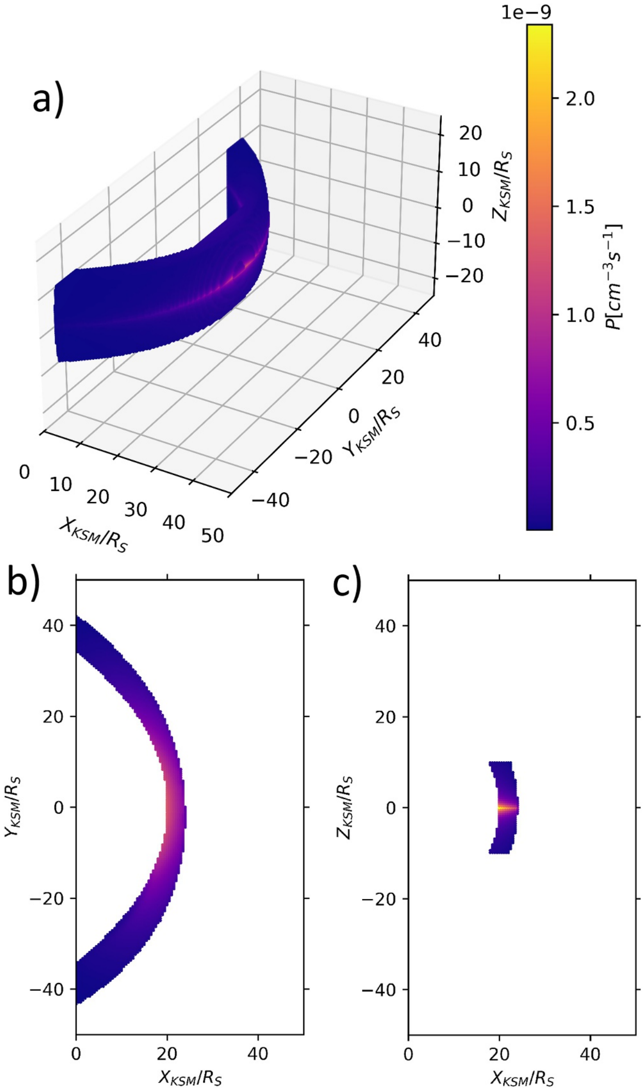

Figure 3. X-ray volumetric photon emission rate P in 3D magnetosheath (a), in equatorial plane slice at $Z = 0$ (b), and in polar slice at $Y = 0$ (c). Color bar denotes strength of emissivity, and x, y, and z axes are in units of R_S.

4. Imaging

Imaging opportunities for a future orbiter mission equipped with a suitable X-ray instrument are explored in addition to the 3D structure of soft X-ray emission. We first consider an instrument similar to the SXI (Soft X-ray Imager) on the upcoming Solar wind Magnetosphere Ionosphere Link Explorer (SMILE) mission (Sembay et al., 2024). The instrument mirror gives a field of view (FOV) of 26.5° × 15.5°, and mounts a detector composed of two CCDs, each of 4510 × 4510 square pixels of size 18 μm, with an effective detector area of 9.6 cm^2.

Two imaging techniques are investigated; the first is informed by a method detailed in Sibeck et al. (2018), taking the photon flux per surface area I in $cm^{-2}\ s^{-1}$ as the integral along the line of sight such that

$$I = \int P \frac{d\Omega}{4\pi} dl \tag{11}$$

where P is the volumetric emission rate and $d\Omega = \sin\theta d\theta d\phi$ is the solid angle, in steradians, over which the emission is integrated. Only the photon flux crossing the front hemisphere of a sphere at the instrument distance is considered that is, integration over π in θ and π in ϕ to give a value of 2π. The count rate of photons incident on the instrument per second is I multiplied by the effective area of the detector.

Figure 4 shows the image created by the 3D emission region when projected onto a 2D plane. This gives a map of incident photon flux per unit area as observed by a SMILE-like SXI instrument at a distance of 150 R_S, which was chosen to capture the entire emission region. The image shows clearly the concentration of soft X-ray emission in the equatorial region, and the decline in emission at high latitudes. The larger depth of the flanks in the direction X_{KSM} compensates for their lower emission and results in a nearly uniform band of photon flux lying along the equatorial plane. The peak flux per unit area is at the center, $8.62 \times 10^{-5}\ cm^{-2}\ s^{-1}$, declining to $8.27 \times 10^{-7}\ cm^{-2}\ s^{-1}$ at the edges. With the detector having an area of 9.6 cm^2, the photon flux per second from the central region is 8.28×10^{-4} counts s^{-1}, equivalent to 7.97 counts per 1/4 of Saturn's rotation period. The number of counts per quarter rotation period is hereafter denoted $N_{1/4}$.

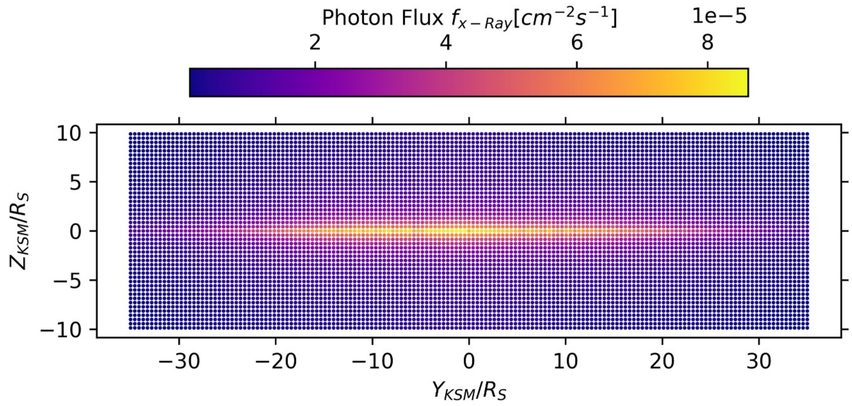

Figure 4. Incident photon flux per unit area for an instrument at distance of 150 R_S, projected onto Y–Z plane.

For comparison, expected background count rates in the soft X-ray band range from 0.12−0.8 counts per second per square degree viewed (Sembay et al., 2024). For the given detector FOV of $26.5° \times 15.5°$, we have a viewing area of $410.75°^2$ and a background count rate of 49.3−329 counts per second, several orders of magnitude larger than the expected count rate from the magnetosheath. This makes the prospect of resolving the whole emission region against this background remote in the extreme.

We conclude that photon flux per pixel is not nearly high enough to allow spatial resolution at a distance where the entire structure is within the detector's field of view, being far below the expected background count rate. At a significantly closer viewing distance of 40 R_S from Saturn, the peak count rate for the spatially resolved case rises to 0.0411 counts s^{-1} (153 $N_{1/4}$) for a SMILE-like instrument. However, the restricted FOV of the instrument means that only a central section representing 0.5% of the magnetosheath emission region is imaged at this distance. Therefore, effective imaging which provides a significant count rate above the soft X-ray background requires either an instrument with a larger effective area, or closer viewing. In a close-viewing case, either a wider FOV or construction of a mosaic of images from a rotating instrument would be necessary to image the full magnetosheath.

The second method models the emission region as a point source (Gustin et al., 2012). For each volume element, the volumetric emission rate P multiplied by the dimensions of the element gives a total emission rate

$$\Gamma = P\delta_x\delta_y\delta_z, \tag{12}$$

where Γ is the number of photons emitted per second by the volume element, and δ_i are the grid spacing of the model in each axis $i = x, y, z$. The emission rate of each volume element is then scaled down by a factor R^2 where R is the distance of the center of the volume element to the instrument in m, giving a received photon rate per unit area in $m^{-2}\ s^{-1}$. This flux rate, multiplied by the detector area, gives the count rate of photons received by the instrument from the whole region when treated as a point source. This opens the possibility for temporal variations in emission to be detected, even if the source cannot be fully spatially resolved.

At a distance of 1,000 R_S, this point source approximation gives a flux per unit area of 0.0103 $cm^{-2}\ s^{-1}$. For the SMILE SXI, the corresponding count rate would be 0.099 counts s^{-1} (954 $N_{1/4}$). Using the small-angle approximation ($\theta < 1°$, where θ is the angular size of the object), the magnetosheath can be treated as a point source from distances larger than 4,600 R_S. Noting that at 1,000 R_S this is a generous approximation, it nonetheless provides an upper estimate for potential soft X-ray detection rates.

The two imaging models were also tested with the Mercury Imaging X-ray Spectrometer (MIXS) on the BepiColombo mission. With a larger effective area of $\sim$50 cm^2 (Martindale et al., 2024), a MIXS-like instrument gives a line of sight count rate in the central region of 4.31×10^{-3} counts s^{-1} (41.51 $N_{1/4}$) at a distance of 150 R_S. At a closer distance of 40 R_S, this count rate would again be higher (0.214 s^{-1}, 799 $N_{1/4}$) Treated as a point source, the count rate at 1,000 R_S is 0.517 s^{-1} (4,970 $N_{1/4}$).

Figure 5 indicates the relationship between viewing distance and count rate for SMILE SXI-like and BepiColombo MIXS-like instruments. Table 3 summarizes our findings, giving count rates per second and per 1/4 rotation of Saturn for both the spatially resolved and point source imaging methods, and for both the SMILE and BepiColombo instruments.

5. Discussion

Soft X-ray emission is generated within Saturn's magnetosheath, however it is not viable to capture an image of the entire region due to low count rates. Imaging spatial features within reasonable system timescales would require instrumentation with a larger effective area or imaging smaller portions of the magnetosheath. This would make it possible to distinguish magnetospheric dynamics and/or neutral density structures.

The Kronian magnetosphere varies on timescales on the order of a rotation period, driven by periodic wave motions in the internal plasma population (Pilkington et al., 2015b). By providing extra internal pressure to oppose the solar wind, such rotation-timescale effects create periodic motion of the magnetopause, which defines the emission region. However, even using a larger-area instrument like MIXS, count rates at 150 R_S are far lower than the soft X-ray background. Spatially resolving this motion is therefore unlikely to be possible, except by

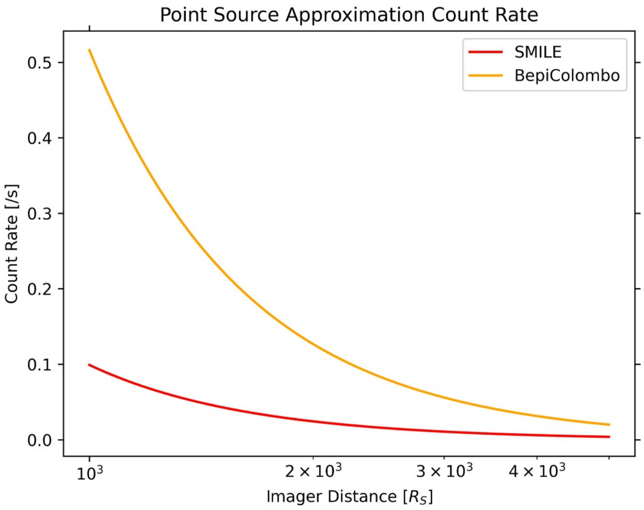

Figure 5. Count rate versus Imaging distance for point source approximation of region, for SMILE (red) and BepiColombo (orange) SXI detectors.

imaging a small portion of the emitting region at a closer distance. Viewed at a far distance (1,000 R_S), this variation in emission over time may be visible when the region is treated as a point source.

The neutral model used in this study extrapolates the neutral density out to the location of the magnetosheath. Data from successful soft X-ray emission observations could be inverted to more accurately constrain the neutral density in the outer system and further refine the model. This could, for example, detect long term variations in the mass ejection rate of Enceladus' plumes, which the neutral model does not account for. Other neutral sources present in the region are not accounted for by this model, and may provide global or local effects on the emission strength of the modeled region. Titan, which is sometimes present in the magnetosheath, is an especially significant H_2 source in the outer system (Tseng et al., 2013), and its contributions could increase emission strength. Dissociation of this H_2 into atomic hydrogen could contribute significantly to the neutral H supply, and thus soft X-ray emission rate, in the outer system. Characterization of other neutral sources in the outer system is less complete, but it is unlikely that Saturn itself (Tseng et al., 2013) or its rings (Shemansky et al., 2009), which are significant in-system hydrogen sources, would have a large impact on the outer system.

The model presented only considers Saturn at equinox. Saturn has an obliquity of 26.7° (Saillenfest et al., 2021). This means that at Winter/Summer Solstice, the equatorial plane of the neutral cloud, aligned with Saturn's rotational axis, will intersect the magnetosheath above/below the nose of the magnetosheath, producing a bright emission band curved above/below the equator, rather than that presented in Figure 4 (Hansen et al., 2005; Pilkington et al., 2015a). We expect that the peak received flux in such configurations to be lower than the results presented here, as the peak of neutral density will no longer align with the peak of plasma density and temperature. Further work could expand this model to consider other geometries.

Significant variation in the location of the magnetosheath, and the composition of its plasma, can also be driven by the different properties of slow and fast modes of solar wind. Naylor et al. (2026) explores the effect of solar wind variations, which can include changes in composition (Schwadron & Cravens, 2000), density, bulk flow velocity, composition and ionisation rates (Feldman et al., 2005), and their effects on magnetosheath shape and location, which drive corresponding changes in the emission profile.

Finally, future campaigns to accurately image the source region must necessarily include the identification, filtering, and removal of background sources of X-rays in the visible energy range of the instrument. As discussed previously, Sembay et al. (2024) estimates background count rates in the context of the SMILE mission in the Earth's magnetosphere. Significant background soft X-ray emission is expected from the Sun (Testa & Reale, 2024), with minor contributions from soft X-ray sources beyond the solar system (Snowden et al., 1997). A diffuse soft X-ray background is created both by interaction of the solar wind with interstellar neutrals which drift into the heliosphere (Lallement et al., 2005), and by interstellar sources (Snowden et al., 1998) All these well-characterized X-ray sources must be considered when analyzing real data results from imaging studies, and each will dominate to a different degree depending on the location and orientation of the instrument, and the particular solar wind environment.

Table 3
Received Photon Count Rates per Second and per Quarter Rotation of Saturn ($N_{1/4}$) for the Spatially Resolved Case at 40 and 150 R_S and Point Source Approximation Using the SMILE and BepiColombo SXI Instruments at a Viewing Distance of 1,000 R_S From Saturn

	Spatially resolved (150 R_S)		Spatially resolved (40 R_S)		Point source (1000R_S)	
SW state	Count rate [s^{-1}]	$N_{1/4}$	Count rate [s^{-1}]	$N_{1/4}$	Count rate [s^{-1}]	$N_{1/4}$
SMILE SXI	8.28×10^{-4}	7.97	0.0411	153	0.099	954
BepiColombo MIXS	4.31×10^{-3}	41.51	0.214	799	0.517	4970

6. Conclusions

We present a new 3D model of soft X-ray emission in Saturn's magnetosheath driven by charge-exchange interactions between water-group neutral species (O, H, OH) and highly -stripped O^{7+} oxygen ions. The model uses MHD simulation data to model the flow of incoming solar wind plasma as it forms the magnetosheath around Saturn. Neutrals originating from Enceladus form overlapping tori concentrated in the equatorial plane and stretching out into the magnetosheath. The model is restricted to near-equatorial latitudes, where neutral densities are better characterized. Relative collision velocities are calculated from bulk flow velocities and plasma temperature. Charge exchange interactions are modeled, and the volumetric photon emission rate computed.

The neutral density distribution is the primary driver of magnetosheath emission spatial structure. Emission was found to be strongly restricted to the equatorial plane and to the nose of the magnetosheath, declining quickly above and below the equatorial plane. Flank emission near $x_{KSM} = 0$ was lower than at the nose by a factor of 100, primarily due to the lower neutral density and despite an increased relative collision velocity.

Imaging of the magnetosheath with a SMILE-like soft X-ray imager was also simulated by two methods: by line integration to project the image of the 3D emission region onto a 2D instrument view; and by treating the whole emission region as a point source. In the first, a spatial map of received flux was constructed, by which neutral density and plasma properties could be constrained. This was investigated at 150 R_S from Saturn, the minimum distance to capture the whole emitting structure, given the FOV restrictions of the simulated instrument, and at 40 R_S, where count rates are higher, but only a small section of the magnetosheath is visible. Viewing as a point source was considered from 1,000 R_S, where temporal variation in emission may be visible. Viewing by an instrument with a larger effective area was also considered, and yielded higher count rates for the same distances.

Spatially resolved imaging of Saturn's magnetopause by a SMILE-like instrument is viable only within 40 R_S, where a count rate of 0.0411 s^{-1} is expected for the brightest region. At this close distance, however, the SMILE SXI field of view could only image 0.5% of the emission region. Solutions for spatial resolution include either using an instrument with a much larger effective area, comparable to MIXS, or closer viewing of individual sections of the emission region. Enhancements in field of view would enable more of the magnetosheath to be imaged on few-minute timescales at sufficiently close distances to get a high count rate. Alternately, with a restricted FOV, the instrument could be rotated, and a mosaic of the magnetosheath could be created from a series of images taken at a close distance.

Count rates for viewing as a point source at 1,000 R_S were 954 per quarter rotation of Saturn for the SMILE SXI, and 4970 for the MIXS, which could be sufficient to see temporal variability on timescales on the order of Saturn's rotation period (Kivelson & Jia, 2014). Therefore, while X-ray imaging of the entire structure is likely unable to capture the short-term variable behavior of the Kronian magnetosphere, such variations could be visible from far distances when treating the region as a point source.

Several methods by which the model can be refined have already been discussed: adding other neutral sources besides Enceladus, especially Titan, whose hydrogen emission is likely to be significant in the outer system (Tseng et al., 2013), and which is occasionally present in the magnetosheath (Burne et al., 2023); the exploration of other system geometries, when the magnetosheath is offset at an angle relative to the equatorial plane in which the neutral tori are concentrated (Hansen et al., 2005; Tsyganenko & Andreeva, 2014); and performing more detailed simulations of imaging by the current generation of SXI instruments. Including the full line of sight integration along every direction, background sources, and close imaging of sub-sections of the emission region, would be beneficial for planning future missions.

Conflict of Interest

The authors declare no conflicts of interest relevant to this study.

Availability Statement

Data for the MHD-simulated magnetosheath and soft X-ray emission rate calculated in this region available in the form of two.csv files via Zenodo at the following https://doi.org/10.5281/zenodo.15870824 (Rogan & Ray, 2025).

Acknowledgments

Primary research of P.C.R. conducted at Lancaster University; further work completed while at University of Cologne. L.C.R. was supported by STFC Grant ST/Y002148/1 to Lancaster University. D.N. was supported by an STFC Studentship to Lancaster University.

References

Achilleos, N., Arridge, C. S., Bertucci, C., Jackman, C. M., Dougherty, M. K., Khurana, K. K., & Russell, C. T. (2008). Large-scale dynamics of Saturn's magnetopause: Observations by Cassini. *Journal of Geophysical Research (Space Physics)*, *113*(A11), A11209. https://doi.org/10.1029/2008JA013265

Allen, R. C., Mitchell, D. G., Paranicas, C. P., Hamilton, D. C., Clark, G., Rymer, A. M., et al. (2018). Internal versus external sources of plasma at Saturn: Overview from magnetospheric imaging investigation/charge-energy-mass spectrometer data. *Journal of Geophysical Research: Space Physics*, *123*(6), 4712–4727. https://doi.org/10.1029/2018JA025262

Arridge, C. S., Achilleos, N., Dougherty, M. K., Khurana, K. K., & Russell, C. T. (2006). Modeling the size and shape of Saturn's magnetopause with variable dynamic pressure. *Journal of Geophysical Research: Space Physics*, *111*(A11). https://doi.org/10.1029/2005JA011574

Bodewits, D., Christian, D. J., Torney, M., Dryer, M., Lisse, C. M., Dennerl, K., et al. (2007). Spectral analysis of the Chandra comet survey. *A&A*, *469*(3), 1183–1195. https://doi.org/10.1051/0004-6361:20077410

Burne, S., Bertucci, C., Sergis, N., Morales, L. F., Achilleos, N., Sánchez-Cano, B., et al. (2023). Space weather in the Saturn–Titan system. *The Astrophysical Journal*, *948*(1), 37. https://doi.org/10.3847/1538-4357/acc738

Carter, J. A., & Sembay, S. (2008). Identifying XMM-newton observations affected by solar wind charge exchange. Part I. *A and A*, *489*(2), 837–848. https://doi.org/10.1051/0004-6361:200809997

Carter, J. A., Sembay, S., & Read, A. M. (2011). Identifying XMM-newton observations affected by solar wind charge exchange – Part II. *A and A*, *527*, A115. https://doi.org/10.1051/0004-6361/201015817

Clarke, K. E., Andrews, D. J., Coates, A. J., Cowley, S. W. H., & Masters, A. (2010). Magnetospheric period oscillations of Saturn's bow shock. *Journal of Geophysical Research: Space Physics*, *115*(A5). https://doi.org/10.1029/2009JA015164

Feldman, U., Landi, E., & Schwadron, N. A. (2005). On the sources of fast and slow solar wind. *Journal of Geophysical Research: Space Physics*, *110*(A7). https://doi.org/10.1029/2004JA010918

Gombosi, T. I., Chen, Y., Glocer, A., Huang, Z., Jia, X., Liemohn, M. W., et al. (2021). What sustained multi-disciplinary research can achieve: The space weather modeling framework. *Journal of Space Weather and Space Climate*, *11*, 42. https://doi.org/10.1051/swsc/2021020

Gustin, J., Bonfond, B., Grodent, D., & Gérard, J.-C. (2012). Conversion from HST ACS and STIS auroral counts into brightness, precipitated power, and radiated power for H_2 giant planets. *Journal of Geophysical Research: Space Physics*, *117*(A7). https://doi.org/10.1029/2012JA017607

Hansen, K. C., Ridley, A. J., Hospodarsky, G. B., Achilleos, N., Dougherty, M. K., Gombosi, T. I., & Tóth, G. (2005). Global MHD simulations of Saturn's magnetosphere at the time of Cassini approach. *Geophysical Research Letters*, *32*(20). https://doi.org/10.1029/2005GL022835

Jackman, C. M., Thomsen, M. F., & Dougherty, M. K. (2019). Survey of Saturn's magnetopause and bow shock positions over the entire Cassini mission: Boundary statistical properties and exploration of associated upstream conditions. *Journal of Geophysical Research: Space Physics*, *124*(11), 8865–8883. https://doi.org/10.1029/2019JA026628

Jia, X., Hansen, K. C., Gombosi, T. I., Kivelson, M. G., Tóth, G., DeZeeuw, D. L., & Ridley, A. J. (2012). Magnetospheric configuration and dynamics of Saturn's magnetosphere: A global MHD simulation. *Journal of Geophysical Research: Space Physics*, *117*(A5). https://doi.org/10.1029/2012JA017575

Kanani, S. J., Arridge, C. S., Jones, G. H., Fazakerley, A. N., McAndrews, H. J., Sergis, N., et al. (2010). A new form of Saturn's magnetopause using a dynamic pressure balance model, based on in situ, multi-instrument Cassini measurements. *Journal of Geophysical Research: Space Physics*, *115*(A6). https://doi.org/10.1029/2009JA014262

Kivelson, M. G., & Jia, X. (2014). Control of periodic variations in Saturn's magnetosphere by compressional waves. *Journal of Geophysical Research: Space Physics*, *119*(10), 8030–8045. https://doi.org/10.1002/2014JA020258

Lallement, R., Quémerais, E., Bertaux, J. L., Ferron, S., Koutroumpa, D., & Pellinen, R. (2005). Deflection of the interstellar neutral hydrogen flow across the heliospheric interface. *Science (American Association for the Advancement of Science)*, *307*(5714), 1447–1449. https://doi.org/10.1126/science.1107953

Leppard, F., Patrick, A., Ray, L., Dunn, W. R., Smith, H. T., Yao, Z., et al. (2025). Estimating solar wind charge exchange generated soft X-rays in the Jovian magnetosheath. *Journal of Geophysical Research: Space Physics*, *130*(7), e2024JA033415. https://doi.org/10.1029/2024JA033415

Martindale, A., McKee, M. J., Bunce, E. J., Lindsay, S. T., Hall, G. P., Tikkanen, T. V., et al. (2024). The bepicolombo mercury imaging X-ray spectrometer. In C. Bambi & A. Santangelo (Eds.), *Handbook of X-ray and gamma-ray astrophysics* (pp. 1059–1113). Springer Nature Singapore. https://doi.org/10.1007/978-981-19-6960-7_171

Naylor, D., Ray, L. C., Dunn, W. R., Jasinski, J. M., & Paty, C. (2025). Estimating soft X-ray emission from Uranus's magnetosheath. *Journal of Geophysical Research: Space Physics*, *130*(11), e2025JA034171. https://doi.org/10.1029/2025JA034171

Naylor, D., Ray, L. C., Rogan, P. C., Dunn, W. R., & Smith, H. T. (2026). Soft X-ray emission from Saturn's magnetosheath II: Solar wind driving. *Journal of Geophysical Research: Space Physics*, *131*(5), e2025JA034461. https://doi.org/10.1029/2025JA034461

Pilkington, N. M., Achilleos, N., Arridge, C. S., Guio, P., Masters, A., Ray, L. C., et al. (2015). Asymmetries observed in Saturn's magnetopause geometry. *Geophysical Research Letters*, *42*(17), 6890–6898. https://doi.org/10.1002/2015GL065477

Pilkington, N. M., Achilleos, N., Arridge, C. S., Guio, P., Masters, A., Ray, L. C., et al. (2015). Internally driven large-scale changes in the size of Saturn's magnetosphere. *Journal of Geophysical Research: Space Physics*, *120*(9), 7289–7306. https://doi.org/10.1002/2015JA021290

Pilkington, N. M., Achilleos, N., Arridge, C. S., Masters, A., Sergis, N., Coates, A. J., & Dougherty, M. K. (2014). Polar confinement of Saturn's magnetosphere revealed by in situ Cassini observations. *Journal of Geophysical Research: Space Physics*, *119*(4), 2858–2875. https://doi.org/10.1002/2014JA019774

Raab, W., Branduardi-Raymont, G., Wang, C., Dai, L., Donovan, E., Enno, G., et al. (2016). SMILE: A joint ESA/CAS mission to investigate the interaction between the solar wind and Earth's magnetosphere. In J.-W. A. den Herder, T. Takahashi, & M. Bautz (Eds.), *Space telescopes and instrumentation 2016: Ultraviolet to gamma ray* (Vol. 9905). https://doi.org/10.1117/12.2231984

Rogan, P. C., & Ray, L. (2025). O7+ soft X-ray emission from Saturn's magnetosheath1 I: 3d Modelling from MHD data dataset. *Zenodo*. https://doi.org/10.5281/zenodo.15870824

Saillenfest, M., Lari, G., & Boué, G. (2021). The large obliquity of Saturn explained by the fast migration of Titan. *Nature Astronomy*, *5*(4), 345–349. https://doi.org/10.1038/s41550-020-01284-x

Schwadron, N. A., & Cravens, T. E. (2000). Implications of solar wind composition for cometary X-rays. *The Astrophysical Journal*, *544*(1), 558–566. https://doi.org/10.1086/317176

Sembay, S., Alme, A. L., Agnolon, D., Arnold, T., Beardmore, A., Margeli, A. B. B., et al. (2024). The soft X-ray imager (SXI) on the smile mission. *Earth and Planetary Physics*, *8*(1), 5–14. https://doi.org/10.26464/epp2023067

Shemansky, D., Liu, X., & Melin, H. (2009). The Saturn hydrogen plume. *Planetary and Space Science*, *57*(14), 1659–1670. https://doi.org/10.1016/j.pss.2009.05.002

Sibeck, D. G., Allen, R., Aryan, H., Bodewits, D., Brandt, P., Branduardi-Raymont, G., et al. (2018). Imaging Plasma density structures in the soft X-Rays generated by solar wind charge exchange with neutrals. *Space Science Reviews*, *214*(4), 79. https://doi.org/10.1007/s11214-018-0504-7

Smith, H. T., Johnson, R. E., Perry, M. E., Mitchell, D. G., McNutt, R. L., & Young, D. T. (2010). Enceladus plume variability and the neutral gas densities in Saturn's magnetosphere. *Journal of Geophysical Research: Space Physics*, *115*(A10). https://doi.org/10.1029/2009JA015184

Smith, H. T., & Richardson, J. D. (2021). The 3d structure of Saturn magnetospheric neutral Tori produced by the Enceladus plumes. *Journal of Geophysical Research: Space Physics*, *126*(3), e2020JA028775. https://doi.org/10.1029/2020JA028775

Snowden, S. L., Egger, R., Finkbeiner, D. P., Freyberg, M. J., & Plucinsky, P. P. (1998). Progress on establishing the spatial distribution of material responsible for the 1/4 kev soft X-ray diffuse background local and halo components. *The Astrophysical Journal*, *493*(2), 715–729. https://doi.org/10.1086/305135

Snowden, S. L., Egger, R., Freyberg, M. J., McCammon, D., Plucinsky, P. P., Sanders, W. T., et al. (1997). Rosat survey diffuse X-ray background maps. II. *The Astrophysical Journal*, *485*(1), 125–135. https://doi.org/10.1086/304399

Sulaiman, A. H., Jia, X., Achilleos, N., Sergis, N., Gurnett, D. A., & Kurth, W. S. (2017). Large-scale solar wind flow around Saturn's non-axisymmetric magnetosphere. *Journal of Geophysical Research: Space Physics*, *122*(9), 9198–9206. https://doi.org/10.1002/2017JA024595

Testa, P., & Reale, F. (2024). The solar X-ray Corona. In C. Bambi & A. Santangelo (Eds.), *Handbook of X-ray and gamma-ray astrophysics* (pp. 3075–3112). Springer Nature Singapore. https://doi.org/10.1007/978-981-19-6960-7_77

Thomsen, M. F., Reisenfeld, D. B., Delapp, D. M., Tokar, R. L., Young, D. T., Crary, F. J., et al. (2010). Survey of ion plasma parameters in Saturn's magnetosphere. *Journal of Geophysical Research (Space Physics)*, *115*(A10), A10220. https://doi.org/10.1029/2010JA015267

Tseng, W.-L., Johnson, R., & Ip, W.-H. (2013). The atomic hydrogen cloud in the Saturnian system. *Planetary and Space Science*, *85*, 164–174. https://doi.org/10.1016/j.pss.2013.06.005

Tsyganenko, N. A., & Andreeva, V. A. (2014). On the "bowl-shaped" deformation of planetary equatorial current sheets. *Geophysical Research Letters*, *41*(4), 1079–1084. https://doi.org/10.1002/2014GL059295

Went, D. R., Hospodarsky, G. B., Masters, A., Hansen, K. C., & Dougherty, M. K. (2011). A new semiempirical model of Saturn's bow shock based on propagated solar wind parameters. *Journal of Geophysical Research: Space Physics*, *116*(A7). https://doi.org/10.1029/2010JA016349

Whittaker, I. C., Sembay, S., Carter, J. A., Read, A. M., Milan, S. E., & Palmroth, M. (2016). Modeling the magnetospheric X-ray emission from solar wind charge exchange with verification from XMM-newton observations. *Journal of Geophysical Research: Space Physics*, *121*(5), 4158–4179. https://doi.org/10.1002/2015JA022292

Yoshino, T., Mitsuda, K., Yamasaki, N. Y., Takei, Y., Hagihara, T., Masui, K., et al. (2009). Energy spectra of the soft X-ray diffuse emission in fourteen fields observed with Suzaku. *Publications of the Astronomical Society of Japan*, *61*(4), 805–823. https://doi.org/10.1093/pasj/61.4.805